Anisotropic magnetism and electronic properties of the kagome metal SmV$_6$Sn$_6$

Xing Huang, Zhiqiang Cui, Chaoxin Huang, Mengwu Huo, Hui Liu, Jingyuan Li, Feixiang Liang, Lan Chen, Hualei Sun, Bing Shen, Yunwei Zhang, and Meng Wang [*]

Center for Neutron Science and Technology, Guangdong Provincial Key Laboratory of Magnetoelectric Physics and Devices, School of Physics, Sun Yat-Sen University, Guangzhou 510275, China

Kagome magnets are expected to feature emergent properties due to the interplay among geometry, magnetism, electronic correlation, and band topology. The magnetism and topological electronic states can be tuned via the rare-earth engineering in RV$_6$Sn$_6$ kagome metals, where R is a rare-earth element. Herein, we present the synthesis and characterization of SmV$_6$Sn$_6$, a metal with two-dimensional kagome nets of vanadium and a frustrated triangular Sm lattice. Some of the Sm atoms are shifted from the normal R positions by $c/2$ along the c axis. Magnetic measurements reveal obvious anisotropy, where the easy magnetic axis is within the ab plane. Electronic transport shows multiband behaviors below 200 K. Density functional theory calculations find that the electronic structure of SmV$_6$Sn$_6$ hosts flat bands, Dirac cones, and saddle points arising from the V $3d$ electrons near the Fermi level. No evidence for the existence of a charge density wave or magnetic order down to 2 K can be observed. Thus, SmV$_6$Sn$_6$ can be viewed as a modest disordered derivative of the RV$_6$Sn$_6$ structure, in which the disordered rare-earth ions can suppress the magnetic order and charge density wave in the RV$_6$Sn$_6$ kagome family.

I. INTRODUCTION

Kagome materials RM_6X_6 (R = rare earth, M = transition metal, X = Sn, Ge) have drawn considerable attention in condensed matter physics due to their rich exotic magnetic and electronic properties [1–11]. These materials feature ideal kagome layer structures consisting of pure transition metals and naturally exhibit Dirac cones, saddle points, and flat bands that are characteristic electronic features of a kagome lattice [1,4,12–14]. For a magnetic kagome system, such as RMn$_6$Sn$_6$, the magnetic structure of the Mn sublattice can be flexibly modulated by the rare earth R bearing different $4f$ moments and ion anisotropy. When R = Gd to Ho, ferrimagnetic (FIM) structures are formed, while antiferromagnetic (AFM) structures are formed when R = Er, Tm, and Lu [3,15]. In YMn$_6$Sn$_6$, frustrated interplanar exchange interactions were suggested to trigger strong magnetic fluctuations, resulting in a complex magnetic phase diagram [16–18]. Of particular interest, a spin-orbit-coupled kagome lattice with strong out-of-plane magnetization can achieve spin-polarized Dirac dispersion with a large Chern gap in TbMn$_6$Sn$_6$ [2]. The Chern-gapped Dirac fermions will host a large Berry curvature and contribute to anomalous electronic and thermal transport effects [2,19,20]. Furthermore, rare-earth magnetism can effectively engineer the Chern gap and related Hall conductivity [3].

Compared with robust magnetically ordered RMn$_6$Sn$_6$, RV$_6$Sn$_6$ compounds solely exhibit weak magnetic couplings among the local $4f$ moments of the R sublattice. RV$_6$Sn$_6$ compounds undergo magnetic ordering transitions at rather low temperatures. The ordering temperature is below 6 K for R = Gd-Ho, while no magnetic ordering is observed down to 1.8 K for R = Er-Yb [5,21–26]. The crystalline electric field (CEF) of rare-earth ions is suggested to play an important role in the development of magnetic anisotropy [5,24]. Topologically nontrivial Dirac surface states (GdV$_6$Sn$_6$ and HoV$_6$Sn$_6$) [1,22,27], quantum oscillation (YV$_6$Sn$_6$) [22], quantum critical behavior (YbV$_6$Sn$_6$) [25], and charge density waves (CDWs) (ScV$_6$Sn$_6$) [14,28,29] have been realized in the RV$_6$Sn$_6$ system. These results suggest that the R sublattice plays an important role in tuning the magnetic and electronic properties of RV$_6$Sn$_6$, driving us to explore the R-site substitution. RM_6X_6 with light R may stabilize crystal and magnetic structures in another way. For example, SmMn$_6$Sn$_6$ and SmFe$_6$Sn$_6$ show HoFe$_6$Sn$_6$- and YCo$_6$Ge$_6$-type structures, respectively [30]. Furthermore, SmMn$_6$Sn$_6$ displays ferromagnetism and a large intrinsic anomalous Hall effect [31].

In this paper, we report the crystal growth, structure, magnetism, electronic transport properties, and band structure calculations of a newly discovered kagome metal SmV$_6$Sn$_6$. Differing from the HfFe$_6$Ge$_6$-type structure of RV$_6$Sn$_6$ (R = Gd-Lu, Y, Sc), SmV$_6$Sn$_6$ crystallizes in the hexagonal SmMn$_6$Sn$_6$ prototype [32]. No evidence for magnetic order and CDW can be observed above 2 K, which may be ascribed to the structural disorders of Sm. As a result of the CEF effect, the easy magnetization direction lies within the ab plane. Electronic transport measurements reveal multiband behaviors arising from the electronic bands of the vanadium kagome sublattice. Density functional theory (DFT) calculations reveal flat bands, Dirac cones, and saddle points for
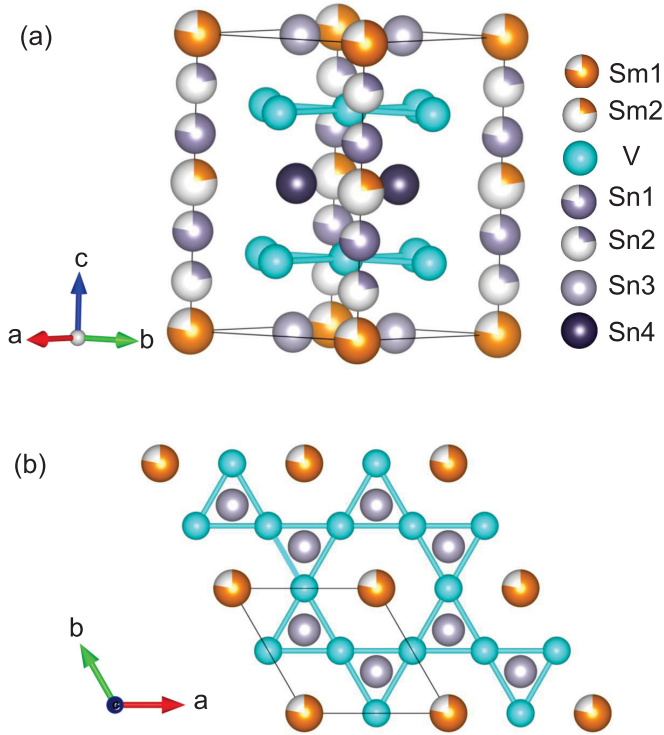
[*]wangmeng5@mail.sysu.edu.cn

FIG. 1. (a) Three-dimensional crystal structure of SmV_6Sn_6. The atom balls with different colors suggest that atoms have fractional occupancy. (b) Top view of the crystal structure, showing the kagome lattice consisting of V atoms.

the kagome V $3d$ bands. The results highlight the interplay between the structural geometry, magnetism, and electronic correlations.

II. EXPERIMENTAL AND CALCULATION DETAILS

Single crystals of SmV_6Sn_6 were grown by the flux method [22]. The starting elements with a molar ratio of Sm:V: Sn = 1:6:40 were loaded in an alumina crucible and sealed in an evacuated silica ampoule. The ampoule was heated to $1100\,°C$ and held for 1 day, then cooled slowly at $3\,°C/h$ to $650\,°C$. The ampoule was taken out and loaded into a centrifuge quickly to separate the excess Sn flux. A dilute HCl solution was used to remove the residual Sn from the crystal surface. The obtained single crystals have a typical size of $2\times1.5\times0.1$ mm^3 as shown in the inset of Fig. 2(a).

Single-crystal x-ray diffraction (XRD) was conducted on a Bruker APEX-II CCD x-ray diffractometer at 150 K. The powder XRD pattern of a crushed single crystal was collected on a powder XRD diffractometer (Empyrean) at room temperature. The elemental analysis was carried out using an energy dispersive x-ray spectroscopy (EDX) (EVO, Zeiss). Magnetic and electronic transport properties were measured on a physical property measurement system (Quantum Design). The in-plane resistivity was measured using the standard four-probe method.

DFT calculations for the structural relaxation and further electronic properties of SmV_6Sn_6 were performed using the Vienna *ab initio* simulation package (VASP 5.4.4) [33]. The

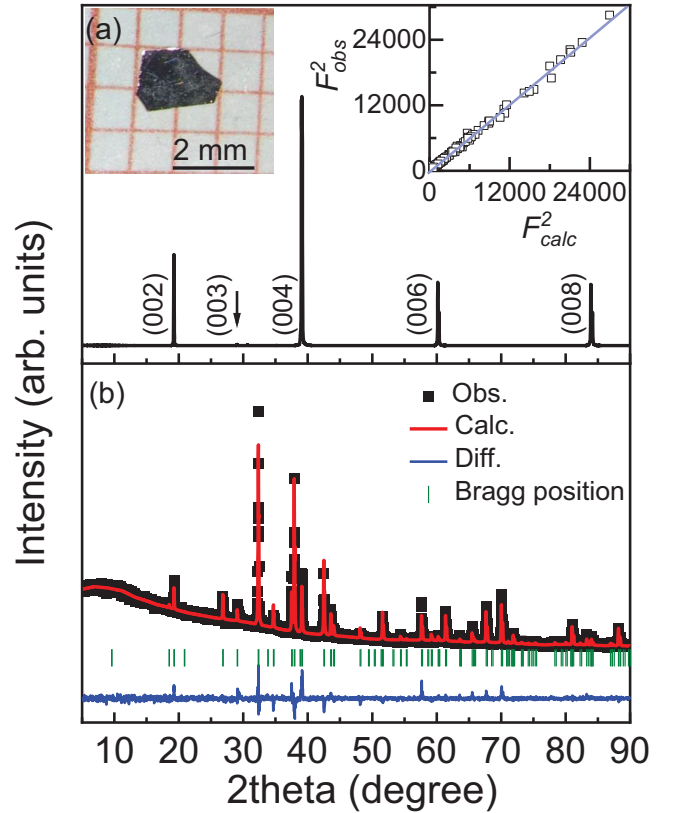FIG. 2. (a) XRD measurement on the *ab* plane of a single crystal of SmV_6Sn_6. The inset on the left is a picture of the single crystal and the right inset shows the refinement of single-crystal diffraction. (b) A pattern of XRD measured on powder samples.

exchange and correlation function was described using the Perdew-Burke-Ernzerhof generalized gradient approximation [34]. The all-electron projector augmented-wave method [35] was adopted to describe the electron-ion interactions, treating $5s^25p^2$, $3d^34s^2$, and $5s^25p^64f^55d^16s^2$ as valence electrons for Sn, V, and Sm atoms, respectively. To ensure convergence of the total energy within a precision of 1 meV per atom, the plane-wave energy cutoff was set at 500 eV, and the Monkhorst-Pack [36] k-point grids with a reciprocal space resolution of $2\pi\times0.03$ Å^{-1} in the Brillouin zone were selected. Structural relaxations were performed with forces converged to less than 0.001 eV Å^{-1}.

III. RESULTS AND DISCUSSIONS

A. Crystal structure

Single-crystal XRD measurements reveal SmV_6Sn_6 crystallizes in the hexagonal space group $P6/mmm$ as that of the $SmMn_6Sn_6$ [32], as shown in Fig. 1. The ideal V kagome layers are separated by Sm and Sn atoms. The refined structural parameters were summarized in Table I. The measured structure factors are in good agreement with the calculated structure factors as shown in the inset of Fig. 2(a).

The results yield 22% of the Sm ions occupying on the intermediate lattice positions ($1b$ site) that are shifted from the Sm positions ($1a$) by $c/2$ along the c axis. The Sm ions on the intermediate sites enforce the nearest-neighbor Sn ions

TABLE I. Crystal parameters of SmV_6Sn_6 from the single-crystal XRD at 150 K (Ga $K\alpha$, $\lambda = 1.341\,38$ Å).

Formula	SmV_6Sn_6	Occupancy
Space group	$P6/mmm$	
a (Å)	5.5243(6)	
c (Å)	9.188(2)	
Sm1	$1a(0, 0, 0)$	0.78
Sm2	$1b(0, 0, 1/2)$	0.22
V	$6i(0, 0, 1/4)$	1
Sn1	$2e[0, 0, 0.3356(2)]$	0.78
Sn2	$2e[0, 0, 0.1673(9)]$	0.22
Sn3	$2c(1/3, 2/3, 0)$	1
Sn4	$2d(1/3, 2/3, 1/2)$	1
Goodness of fit on F^2	1.112	
R_1, wR_2 (all data)	0.0378, 0.0747	

to the Sn2 sites. The occupancy of Sm in both the Sm1 (1a site) and Sm2 (1b site) positions is confirmed by the weaker intensity of the (003) reflection compared with the fully ordered GdV_6Sn_6 and HoV_6Sn_6, as shown in Fig. 2(a) [1]. The shift of the R atoms has also been observed in the other RM_6Sn_6 systems, where R are light rare-earth elements [30,32]. Following the lanthanide contraction rule, the lattice constants a and c in SmV_6Sn_6 are larger than that of the heavy rare-earth elements, indicating the Sm ions are trivalent [5]. Thus, SmV_6Sn_6 can be regarded as a modest disordered derivative of the RV_6Sn_6 (R = Gd-Lu, Y, Sc) structure. The powder XRD pattern in Fig. 2(b) further confirms that no impurity could be identified within our instrumental resolution. Furthermore, the EDX measurements yield an atomic ratio of Sm : V : Sn = 1 : 6.79 : 6.62, close to the stoichiometry of SmV_6Sn_6.

B. Magnetic properties

Figure 3(a) shows magnetic susceptibility [$\chi(T)$] measured with a 0.6 T magnetic field. No obvious furcation exists between zero-field-cooled (ZFC) and field-cooled (FC) susceptibility curves. The $\chi(T)$ along the ab plane is larger than that along the c axis at low temperatures, revealing a strong easy-plane anisotropy. The magnetic susceptibility increases rapidly and large anisotropy is developed below 10 K, consistent with the development of short-range magnetic order. No evidence for a magnetic ordering transition appears down to 2 K from susceptibility measured under in-plane magnetic fields, as shown in Fig. 3(b). The Curie-Weiss susceptibility considering the Van Vleck contribution follows the expression $\chi = C/(T - \theta_{CW}) + \chi_{VV}$, where θ_{CW} is the Curie-Weiss temperature, C is the Curie constant, and χ_{VV} is the temperature-independent Van Vleck contribution [37]. As the inset shown in Fig. 3(a), the susceptibility at high temperatures deviates from the Curie-Weiss behavior, suggesting the involvement of the crystal field effect of Sm^{3+}. To get the effective magnetic exchange interactions, we fit the susceptibility using the Curie-Weiss formula from 25 to 50 K, resulting in $\theta_{CW}^{ab} = 4.9(7)$ K, $C^{ab} = 4(2) \times 10^{-2}$ emu K mol^{-1} Oe^{-1}, and $\chi_{VV} = 4.3(3) \times 10^{-4}$ emu mol^{-1} Oe^{-1} for the $H \parallel ab$ plane, and $\theta_{CW}^c = -6(3)$ K, $C^c = 3.6(6) \times 10^{-2}$ emu K mol^{-1} Oe^{-1}, and
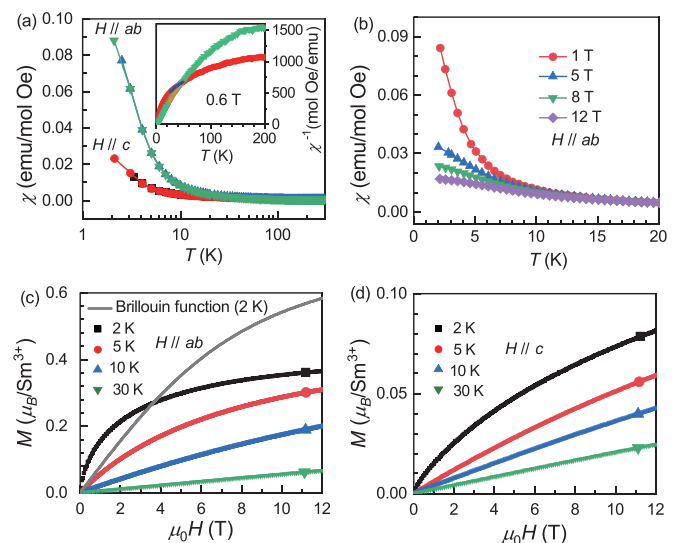

FIG. 3. (a) Temperature dependence of zero-field-cooled (ZFC) and field-cooled (FC) magnetic susceptibilities measured with a 0.6 T magnetic field along the c axis and ab plane of SmV_6Sn_6. The blue and orange lines indicate a Curie-Weiss fit to the inverse susceptibility data from 25 to 50 K. (b) Magnetic susceptibilities measured with various magnetic fields along the ab plane. (c) Magnetization against magnetic fields along the c axis and (d) the ab plane at 2, 5, 10, and 30 K. The Brillouin function (gray line) in (c) is for $J = 5/2$ (Sm^{3+}) and $T = 2$ K.

$\chi_{VV} = 8.4(7) \times 10^{-4}$ emu mol^{-1} Oe^{-1} for the $H \parallel c$ axis. The positive θ_{CW}^{ab} suggests a dominant ferromagnetic (FM)-type in-plane magnetic interaction while the negative θ_{CW}^c shows AFM-type out-of-plane interactions. The effective magnetic moments of Sm^{3+} ions are calculated to be $\mu_{eff}^{ab} = 0.605(1)\mu_B$ and $\mu_{eff}^c = 0.536(1)\mu_B$, which are smaller than $0.845\mu_B$ of a free Sm^{3+} ion ($J = 5/2$, $g = 2/7$). The reduced effective moments are also observed in the other samarium compounds such as $Sm_3Sb_3Zn_2O_{14}$ ($0.53\mu_B$) [38] and $Sm_2Zr_2O_7$ ($0.5\mu_B$) [39], which are likely related to the narrow J multiplet width arising from the large crystal field splitting of the lowest $J = 5/2$ multiplets.

Isothermal magnetization data at different temperatures are plotted in Figs. 3(c) and 3(d). Large magnetic anisotropy can be observed at low temperatures. The magnetization for the $H \parallel ab$ plane is about 4.5 times larger than that for $H \parallel c$ at 2 K. When the field is parallel to the ab plane at 2 K, the magnetization increases linearly in the low field and then gradually approaches saturation. The magnetization is up to $0.37\mu_B$ at 12 T, which is far smaller than the theoretical value of $M_s = gJ = 0.71\mu_B$. As a comparison, we plot the Brillouin function that describes the magnetization of the paramagnetic state of SmV_6Sn_6 in Fig. 3(c). The values of the Brillouin function in the magnetic field lower than 3.6 T are smaller than the magnetization for the $H \parallel ab$ plane and larger than that for $H \parallel c$ axis, consistent with the FM in-plane interactions and AFM out-of-plane interactions. For larger magnetic fields ($\mu_0H > 3.6$ T) and higher temperatures ($T > 10$ K), the magnetic properties in the paramagnetic state are governed by the crystal field effect of Sm^{3+}.
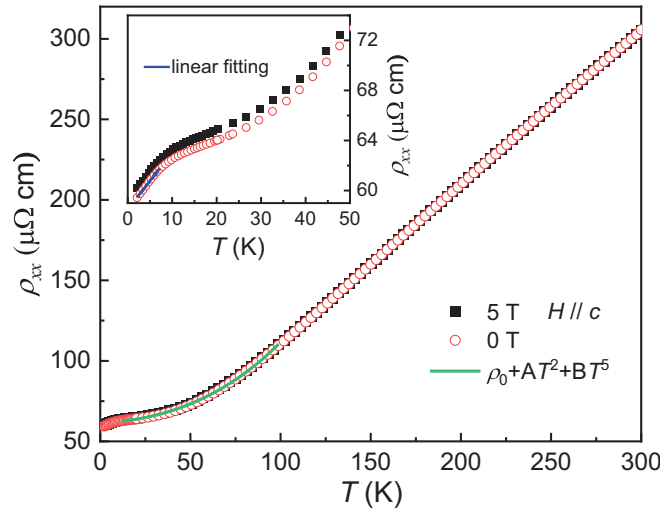
FIG. 4. Resistivity of SmV_6Sn_6 measured at 0 and 5 T magnetic fields. The green curve shows the fitting of $\rho_{xx}(T)$ via the equation $\rho = \rho_0 + AT^2 + BT^5$. The inset is a zoom-in resistivity at low temperatures. The solid line is a linear fitting below 7 K.

C. Transport properties

Figure 4 shows the temperature dependence of the in-plane resistivity $\rho_{xx}(T)$ at 0 and 5 T magnetic fields. The resistivity decreases with decreasing temperature, consistent with the characteristic of a metal. The resistivity in the temperature range of 10–100 K follows $\rho = \rho_0 + AT^2 + BT^5$, giving rise to $\rho_0 = 61.5(1)$ μΩ cm, $A = 4.4(1) \times 10^{-3}$ μΩ cm K^{-2}, and $B = 5.1(7) \times 10^{-10}$ μΩ cm K^{-5}. The terms AT^2 and BT^5 represent the contributions from electron and phonon scatterings, respectively. The inset of Fig. 4 displays a decrease of resistivity below 10 K, which may be related to the formation of short-range magnetic order. In addition, the resistivity is enhanced by a 5 T magnetic field at low temperatures. The resistivity changes linearly between 2 and 7 K, indicating the existence of weak spin fluctuations.

To study the magnetoresistance (MR) effect, we further measured the field dependence of the longitudinal resistivity [$\rho_{xx}(H)$] at various temperatures. The MR defined as $[\rho_{xx}(H) - \rho_{xx}(H = 0)]/\rho_{xx}(H = 0) \times 100\%$ is shown in Fig. 5(a). The current is along the ab plane and the magnetic field is along the c axis. A small magnitude of MR can be observed at all temperatures. The MR does not tend to saturate up to 12 T. The MR is gradually increased with decreasing temperature. However, a small decrease can be found at 2 K compared with that of 30 K, which may be a consequence of suppressed spin-disorder scattering.

To characterize the carrier concentrations and effective mobilities, Hall resistance [$\rho_{xy}(H)$] measurements were performed from 2 to 300 K with the magnetic field applied parallel to the c axis and the current within the ab plane as shown in Fig. 5(b). The $\rho_{xy}(H)$ curves are linear at temperatures $T \geqslant 250$ K. The ρ_{xy} decreases nonlinearly as the temperature decreases below 250 K, signifying a multiband transport behavior. The $\rho_{xy}(H)$ curves can be fitted with a single-band model at high temperatures ($T \geqslant 250$ K) and a two-band model at low temperatures ($T < 250$ K).
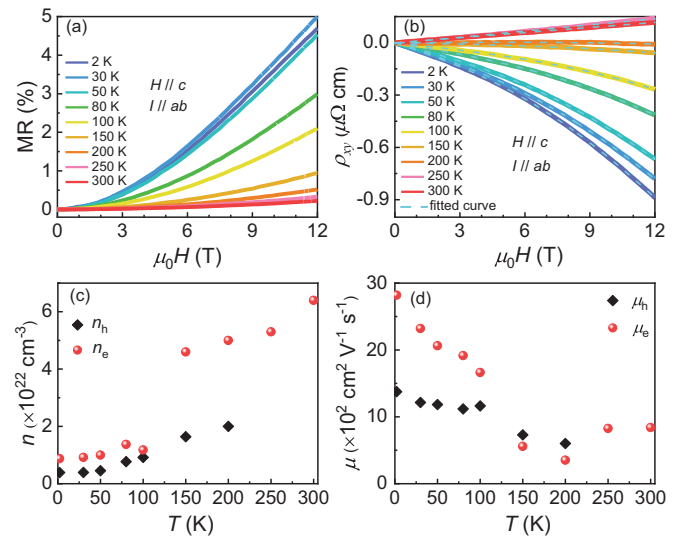

FIG. 5. (a) Magnetoresistance at various temperatures measured with the $H \parallel c$ axis. The magnetoresistance component was isolated by averaging $\rho_{xx}(H)$ and $\rho_{xx}(-H)$. (b) Hall resistivity ρ_{xy} measured at different temperatures. To remove the effects of the longitudinal resistivity, ρ_{xy} is obtained via $\rho_{xy} = [\rho_{xy}(H) - \rho_{xy}(-H)]/2$. (c) Carrier densities of electrons and holes obtained from fitting of the Hall resistivity in (b) with a two-band model below 250 K and a single-band model for higher temperatures. (d) Charge carrier mobilities against temperature obtained from fitting the Hall resistivity.

Figures 5(c) and 5(d) display the fitted results. It can be found that the concentration and mobility of the electron carriers are larger than that of the holes for most temperatures, suggesting that electrons play a dominant role in conduction. The similar multiband transport behaviors have also been observed in RV_6Sn_6 ($R = $ Gd-Lu, Y) [22,24,26].

D. Electronic structure

It is difficult to calculate the electronic structure via the DFT for the compound with disorders. We constructed two types of crystal structures via rearranging the atomic occupancies of the Sm and Sn sites in SmV_6Sn_6. For the type-1 structure, the atomic occupancies of both the Sm1 and Sn1 sites are 100%; for the type-2 structure, Sm and Sn fully occupy the Sm2 and Sn2 sites, respectively. The experimentally synthesized SmV_6Sn_6 can be regarded as an intermediate phase of the type-1 and type-2 structures. Figures 6(c)–6(f) show that the two types of structures possess similar electronic structures, suggesting the synthesized SmV_6Sn_6 has an approximative electronic structure. The orbital projected density of states yields that the $3d$ electrons of V atoms make a dominant contribution near the Fermi level. The electronic band structures are shown in Figs. 6(e) and 6(f), where an obvious kagome flat band characterized by the V d_{z^2} orbitals can be observed above E_F. Moreover, the Dirac cones and saddle points appear at the K and M points, respectively, as expected from minimal kagome tight-binding models [40]. Such a transition-metal-based d-orbital band structure endemic to the kagome lattice in the proximity of the Fermi level is one of the common features in the family of RM_6Sn_6 [1,4,12–14].
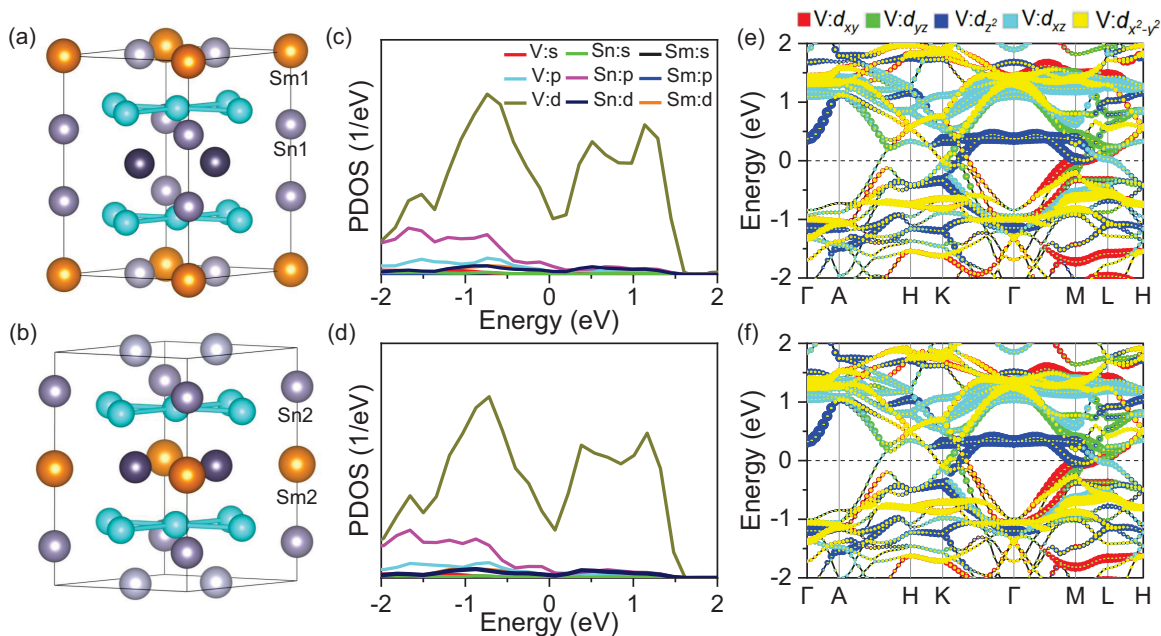
FIG. 6. (a) Sketch of the type-1 structure with fully occupied Sm1 and Sn1 sites. (b) Sketch of the type-2 structure with Sm and Sn occupying the Sm2 and Sn2 sites. (c) Orbital projected density of states of type-1 and (d) type-2 structures. (e) and (f) V d orbital decomposed band structures.

IV. DISCUSSIONS

Compared with the RM_6X_6 ($M = $ Mn, Fe, $X = $ Ge, Sn) family with magnetic ordering temperatures originating from the transition metals well above room temperature [6,7,11], the moments of the rare-earth ions in RV_6Sn_6 ($R = $ Gd-Ho) order at rather low temperatures [5]. The magnetic transition temperatures of RV_6Sn_6 are affected by the CEF of the R ions. The leading crystal field parameter B_2^0 can be calculated via the point charge model $B_2^0 = 10(\theta_{CW}^{ab} - \theta_{CW}^c)/3(2J - 1)$ $(2J + 3)$, giving rise to $B_2^0 = 1.48$ K for SmV_6Sn_6. The positive value is close to that of TmV_6Sn_6 [5], which shows an easy in-plane anisotropy. Normally, a large B_2^0 with strong CEF as -1.4 K of TbV_6Sn_6 is expected to enhance the magnetic ordering temperature [5]. However, the magnetic order has not been observed down to 2 K in SmV_6Sn_6. The absence of magnetic order may be related to the atomic disorder associated with the shifts of the Sm^{3+} ions along the c axis.

The DFT calculations reveal that the flat bands at the Γ point of the type-1 and type-2 structures are located at 0.376 and 0.326 eV, respectively. The difference should be associated with the strength of V d–Sn p orbital hybridization. The different V-Sn1 [2.872(1) Å] and V-Sn2 [2.865(3) Å] bond lengths will result in different strengths of orbital hybridization. It was reported that ScV_6Sn_6 undergoes a CDW phase transition at 92 K, in which the V-Sn bond length is 2.822(1) Å [28], while no evidence of CDW is observed in the isostructural RV_6Sn_6 compounds with the larger ions $R = $ Y, Sm-Lu [5,25]. The V-Sn bond length in the RV_6Sn_6 family depends on the chemical pressure arising from the rare-earth ions R^{3+}. The smaller ion radius of R^{3+}, the shorter is the bond length. Recent studies suggested that the exotic CDW in ScV_6Sn_6 is not Fermi-surface nesting driven. The structural degree of freedom may play a fundamental role in stabilizing

the CDW [41–44]. Large modulated displacements of Sc and Sn atoms have been observed, which can be attributed to the small Sc atomic radius [45]. Thus, further explorations for smaller R systems or the effect of pressure are interesting for investigations of the interplays among lattice, charge, and magnetism.

V. CONCLUSIONS

Single crystals of the kagome metal SmV_6Sn_6 have been grown by the self-flux method. The crystal structure of SmV_6Sn_6 belongs to the $SmMn_6Sn_6$ prototype, showing partial crystallographic disorder associated with the appearance of an additional Sm site. Large magnetic anisotropy due to the CEF effects is found for the magnetic Sm^{3+} ions. Moments tend to align in the ab plane. No abnormal transition related to long-range magnetic ordering and CDW can be observed down to 2 K. Electronic transport measurements exhibit multiband behaviors and positive magnetoresistance properties. DFT calculations show a V $3d$ kagome band structure near the Fermi level with a flat band, Dirac cones, and saddle points.

[1] S. Peng, Y. Han, G. Pokharel, J. Shen, Z. Li, M. Hashimoto, D. Lu, B. R. Ortiz, Y. Luo, H. Li *et al.*, Phys. Rev. Lett. **127**, 266401 (2021).

[2] J.-X. Yin, W. Ma, T. A. Cochran, X. Xu, S. S. Zhang, H.-J. Tien, N. Shumiya, G. Cheng, K. Jiang, B. Lian *et al.*, Nature (London) **583**, 533 (2020).

[3] W. Ma, X. Xu, J.-X. Yin, H. Yang, H. Zhou, Z.-J. Cheng, Y. Huang, Z. Qu, F. Wang, M. Z. Hasan *et al.*, Phys. Rev. Lett. **126**, 246602 (2021).

[4] M. Li, Q. Wang, G. Wang, Z. Yuan, W. Song, R. Lou, Z. Liu, Y. Huang, Z. Liu, H. Lei *et al.*, Nat. Commun. **12**, 3129 (2021).

[5] J. Lee and E. Mun, Phys. Rev. Mater. **6**, 083401 (2022).

[6] G. Venturini, R. Welter, and B. Malaman, J. Alloys Compd. **185**, 99 (1992).

[7] G. Venturini, B. C. El Idrissi, and B. Malaman, J. Magn. Magn. Mater. **94**, 35 (1991).

[8] X. Teng, L. Chen, F. Ye, E. Rosenberg, Z. Liu, J.-X. Yin, Y.-X. Jiang, J. S. Oh, M. Z. Hasan, K. J. Neubauer *et al.*, Nature (London) **609**, 490 (2022).

[9] P. Schobinger-Papamantellos, J. Rodríguez-Carvajal, and K. Buschow, J. Alloys Compd. **256**, 92 (1997).

[10] A. Szytuła, E. Wawrzyńska, and A. Zygmunt, J. Alloys Compd. **366**, L16 (2004).

[11] X.-L. Rao and J. Coey, J. Appl. Phys. **81**, 5181 (1997).

[12] X. Gu, C. Chen, W. S. Wei, L. L. Gao, J. Y. Liu, X. Du, D. Pei, J. S. Zhou, R. Z. Xu, Z. X. Yin *et al.*, Phys. Rev. B **105**, 155108 (2022).

[13] P. Wang, Y. Wang, B. Zhang, Y. Li, S. Wang, Y. Wu, H. Zhu, Y. Liu, G. Zhang, D. Liu *et al.*, Chin. Phys. Lett. **37**, 087102 (2020).

[14] T. Hu, H. Pi, S. Xu, L. Yue, Q. Wu, Q. Liu, S. Zhang, R. Li, X. Zhou, J. Yuan *et al.*, Phys. Rev. B **107**, 165119 (2023).

[15] B. Wang, E. Yi, L. Li, J. Qin, B.-F. Hu, B. Shen, and M. Wang, Phys. Rev. B **106**, 125107 (2022).

[16] R. L. Dally, J. W. Lynn, N. J. Ghimire, D. Michel, P. Siegfried, and I. I. Mazin, Phys. Rev. B **103**, 094413 (2021).

[17] Q. Wang, K. J. Neubauer, C. Duan, Q. Yin, S. Fujitsu, H. Hosono, F. Ye, R. Zhang, S. Chi, K. Krycka *et al.*, Phys. Rev. B **103**, 014416 (2021).

[18] N. J. Ghimire, R. L. Dally, L. Poudel, D. Jones, D. Michel, N. T. Magar, M. Bleuel, M. A. McGuire, J. Jiang, J. Mitchell *et al.*, Sci. Adv. **6**, eabe2680 (2020).

[19] X. Xu, J.-X. Yin, W. Ma, H.-J. Tien, X.-B. Qiang, P. V. S. Reddy, H. Zhou, J. Shen, H.-Z. Lu, T.-R. Chang, Z. Qu, and S. Jia, Nat. Commun. **13**, 1197 (2022).

[20] H. Zhang, J. Koo, C. Xu, M. Sretenovic, B. Yan, and X. Ke, Nat. Commun. **13**, 1091 (2022).

[21] H. Ishikawa, T. Yajima, M. Kawamura, H. Mitamura, and K. Kindo, J. Phys. Soc. Jpn. **90**, 124704 (2021).

[22] G. Pokharel, S. M. L. Teicher, B. R. Ortiz, P. M. Sarte, G. Wu, S. Peng, J. He, R. Seshadri, and S. D. Wilson, Phys. Rev. B **104**, 235139 (2021).

[23] E. Rosenberg, J. M. DeStefano, Y. Guo, J. S. Oh, M. Hashimoto, D. Lu, R. J. Birgeneau, Y. Lee, L. Ke, M. Yi, and J.-H. Chu, Phys. Rev. B **106**, 115139 (2022).

[24] X. Zhang, Z. Liu, Q. Cui, Q. Guo, N. Wang, L. Shi, H. Zhang, W. Wang, X. Dong, J. Sun *et al.*, Phys. Rev. Mater. **6**, 105001 (2022).

[25] K. Guo, J. Ye, S. Guan, and S. Jia, arXiv:2210.12117.

[26] G. Pokharel, B. Ortiz, J. Chamorro, P. Sarte, L. Kautzsch, G. Wu, J. Ruff, and S. D. Wilson, Phys. Rev. Mater. **6**, 104202 (2022).

[27] Y. Hu, X. Wu, Y. Yang, S. Gao, N. C. Plumb, A. P. Schnyder, W. Xie, J. Ma, and M. Shi, Sci. Adv. **8**, eadd2024 (2022).

[28] H. W. S. Arachchige, W. R. Meier, M. Marshall, T. Matsuoka, R. Xue, M. A. McGuire, R. P. Hermann, H. Cao, and D. Mandrus, Phys. Rev. Lett. **129**, 216402 (2022).

[29] X. Zhang, J. Hou, W. Xia, Z. Xu, P. Yang, A. Wang, Z. Liu, J. Shen, H. Zhang, X. Dong *et al.*, Materials **15**, 7372 (2022).

[30] J. S.-Damm, E. Gałdecka, O. Bodak, and B. Belan, J. Alloys Compd. **298**, 26 (2000).

[31] W. Ma, X. Xu, Z. Wang, H. Zhou, M. Marshall, Z. Qu, W. Xie, S. Jia *et al.*, Phys. Rev. B **103**, 235109 (2021).

[32] B. Malaman, G. Venturini, B. C. El Idrissi, and E. Ressouche, J. Alloys Compd. **252**, 41 (1997).

[33] G. Kresse and J. Furthmüller, Comput. Mater. Sci. **6**, 15 (1996).

[34] J. P. Perdew, E. R. McMullen, and A. Zunger, Phys. Rev. A **23**, 2785 (1981).

[35] G. Kresse and D. Joubert, Phys. Rev. B **59**, 1758 (1999).

[36] H. J. Monkhorst and J. D. Pack, Phys. Rev. B **13**, 5188 (1976).

[37] J. Hodges, P. Bonville, A. Forget, M. Rams, K. Królas, and G. Dhalenne, J. Phys.: Condens. Matter **13**, 9301 (2001).

[38] M. B. Sanders, M. B. Sander, and R. J. Cava, J. Mater. Chem. C **4**, 541 (2016).

[39] S. Singh, S. Saha, S. K. Dhar, R. Suryanarayanan, A. K. Sood, and A. Revcolevschi, Phys. Rev. B **77**, 054408 (2008).

[40] J.-X. Yin, B. Lian, and M. Z. Hasan, Nature (London) **612**, 647 (2022).

[41] Y. Hu, J. Ma, Y. Li, D. J. Gawryluk, T. Hu, J. Teyssier, V. Multian, Z. Yin, Y. Jiang, S. Xu *et al.*, arXiv:2304.06431.

[42] S.-H. Kang, H. Li, W. R. Meier, J. W. Villanova, S. Hus, H. Jeon, H. W. S. Arachchige, Q. Lu, Z. Gai, J. Denlinger *et al.*, arXiv:2302.14041.

[43] M. Tuniz, A. Consiglio, D. Puntel, C. Bigi, S. Enzner, G. Pokharel, P. Orgiani, W. Bronsch, F. Parmigiani, V. Polewczyk *et al.*, arXiv:2302.10699.

[44] S. Cheng, Z. Ren, H. Li, J. Oh, H. Tan, G. Pokharel, J. M. DeStefano, E. Rosenberg, Y. Guo, Y. Zhang *et al.*, arXiv:2302.12227.

[45] H. Tan and B. Yan, arXiv:2302.07922.